

# Phase-resolved measurements on a multi-slotted Synthetic Jets actuator

Giuseppe Ceglia<sup>1\*</sup>, Marco Invigorito<sup>1</sup>, Matteo Chiatto<sup>2</sup>, Carlo Salvatore Greco<sup>2</sup>, Gennaro Cardone<sup>2</sup>, Luigi de Luca<sup>2</sup>

<sup>1</sup>CIRA Italian Aerospace Research Centre, Dept. of Aero-thermodynamic and Combustion, Capua, Italy

<sup>2</sup>Università degli Studi di Napoli “Federico II”, Dept. of Industrial Engineering, Naples, Italy

\*g.ceglia@cira.it

## Abstract

The free flow field of a multi-slotted array of Synthetic Jets (SJ) has been experimentally investigated in quiescent ambient at Reynolds and Strouhal numbers,  $Re = 128$  and  $St = 0.11$ , respectively. The multi-slotted SJ actuator is composed of twelve rectangular slots with an aspect ratio of 15 (for a width of  $\sim 1$  mm) and off-centered with respect to the cavity center. Experiments were conducted at three equally-spaced cross sectional planes inspecting two consecutive slots by means of phase-locked Stereo-Particle Image Velocimetry. At the slot exit, the statistical analysis reveals that the SJ exhibits an asymmetric spreading with respect to the geometrical axis of the slot, being tilted of about  $\sim 14.8^\circ$  on the side where the cavity extends. This asymmetric pattern determines a small recirculation region slightly downstream of the slot exit. On the other hand, the flow field appears two-dimensional at the mid spanwise distance between the two slots. The phase-locked flow fields exhibit counter-rotating vortical patterns that convect downstream from the slot exit during the ejection phase. These vortices develop in longitudinal direction at 3.4 slot widths and then dissipate as they travel further downstream.

## 1 Introduction

Among the various devices developed for active flow control (AFC) applications (Ho and Tai 1996), synthetic jet (SJ) actuators have proven promising features as low-power AFC technology (Glezer and Amitay 2002). The exploitation of the SJs relies upon their mechanism of momentum transfer to the controlled flow without a direct introduction of mass, being zero-net mass-flux actuators. Hence, benefits in design and maintenance are provided by peculiar features such as high efficiency, design-friendly, easy miniaturization. A classical configuration of a SJ actuator consists of a cavity, an oscillating diaphragm and an orifice (Glezer and Amitay 2002). The periodic motion of the diaphragm in the cavity determines a volume change, which in turn produces a pressure variation. Fluid passes through the orifice leading to injection and ejection phases per cycle. During the injection, the diaphragm determines a low pressure in the cavity pulling fluid from the external ambient. Conversely, overpressure in the cavity causes the ejection phase pushing fluid out from the orifice. This forcing can cause trains of consecutive vortical structures that advect away from the orifice exit and eventually synthesize a jet (Smith and Glezer 1998).

Several studies have been focused on the application of SJ devices for flow control purposes (Glezer 2011). SJs have also been used for mitigation or even suppression of the flow separation (Amitay et al. 1998). In particular, the multi-slotted configuration of rectangular SJs represents an attractive solution for a variety of flow control applications (Sahni et al. 2011). Therefore, the focus of the present work is to investigate the flow features of a multi-slotted SJ issuing in a quiescent ambient.

This work is presently being conducted in the framework of the ‘SJ issuing in quiescent ambient’ task pertaining to the Synthetic jet actuators for flow control (SHAFT) project funded by CIRA. SHAFT project aims to design, test and model a SJ device to control the flow over a backward-facing ramp. Its design in terms of geometry and operating conditions has been carried out by means of a lumped-element model described by Chiatto et al. (2017). This multi-slotted configuration was preliminary studied by Palumbo et al. (2018), and the jet formation has been also checked with the procedure outlined by Chiatto et al. (2019). The free flow field of a finite array of SJ has been experimentally investigated at different cross sectional planes by means of phase-locked stereo-particle image velocimetry (S-PIV) (Willert 1999). Phase-resolved measurements have been conducted to unveil the main flow features of the SJs during their evolution.

## 2 Experimental setup

The experiments were conducted at Reynolds number  $Re = 128$  and Strouhal number  $St = 0.11$ , with maximum predicted axial velocity and actuation frequency of approximately 7.3 m/s and 250 Hz, respectively. The non-dimensional numbers are defined in Eq. (1).

$$Re = \frac{U_0 D}{\nu} \text{ and } St = \frac{f D}{U_0} \quad (1)$$

where  $U_0 = 2.32$  m/s is a characteristic velocity computed as the mean velocity over half cycle during the ejection phase,  $\nu$  is the kinematic viscosity,  $f$  is the actuation frequency and  $D$  the slot width (1mm).

The experimental setup is composed of the SJ actuator with its controller and S-PIV experimental arrangement.

### 2.1 Synthetic Jet actuator

SJ apparatus was built by the Department of Industrial Engineering (DII, University of Naples ‘Federico II’) in the framework of the SHAFT CIRA project; the assembly of the SJ actuator is shown in Figure 1. A carrier frame holds three piezo-element actuators, which are enclosed in a front plate equipped with twelve slots of width  $D = 1$  mm disposed in series along the transversal direction. A spacer frame is interposed in order to ensure the proper height of the cavity.

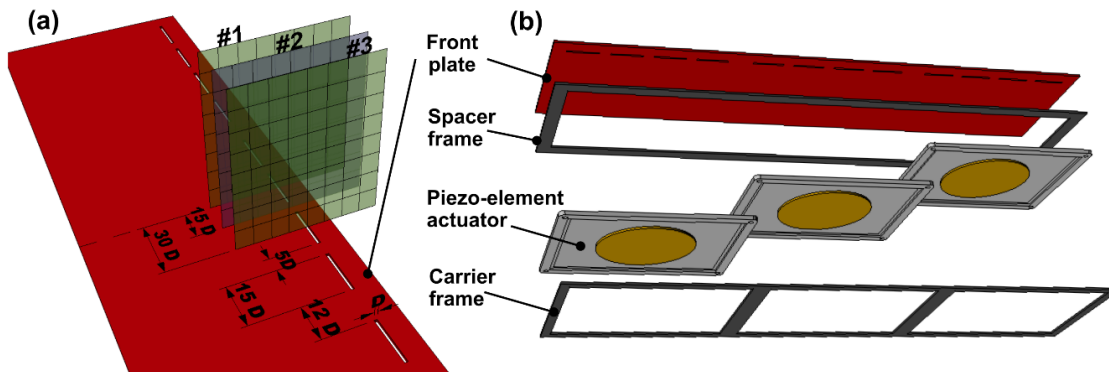


Figure 1 Front plate with 12 slots of width of  $D = 1$  mm and main dimensions; investigated sectional planes (a); Synthetic Jet assembly (from top to bottom): front plate, spacer frame, piezo-element actuators and carrier frame (b).

The device was electrically excited by a sine signal, generated through a multi-function instrument (the Digilent Analog Discovery 2, which can work simultaneously as both signal generator and data-acquisition system) and then transmitted to a linear gain amplifier (EPA-104, Piezo Systems). The actuator and the PIV system were triggered via a signal generator to ensure the measurements synchronization.

## 2.2 PIV measurements and data processing

The present paragraph describes the PIV experimental setup used for the measurements of the SJ issuing in quiescent ambient.

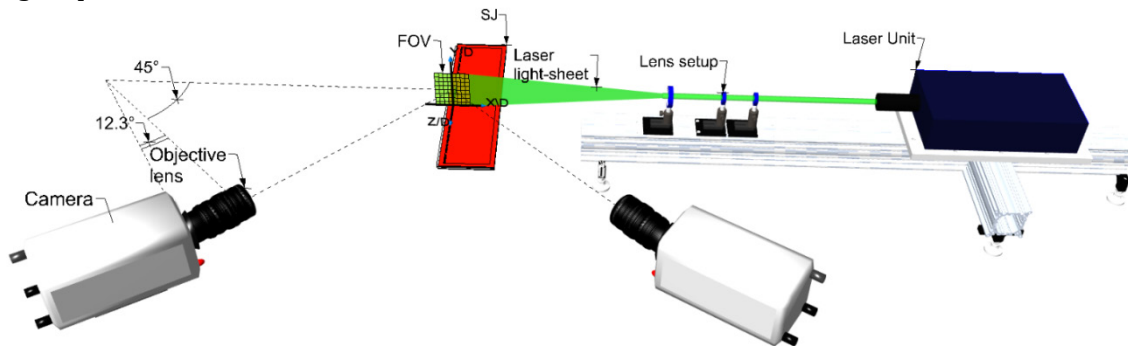


Figure 2 Stereo PIV setup: laser unit, lens setup, SJ actuator, camera system, measurement domain and reference frame.

Figure 2 shows the Stereo PIV experimental setup for the investigation of the X-Y plane at the SJ slot exit. The flow is seeded with oil droplets with a diameter of approximately  $1 \mu\text{m}$  generated by a Laskin nozzle. The Quantel Evergreen laser, a double pulsed Nd:YAG laser (532 nm, 200 mJ per pulse, <10 ns pulse duration), provides the proper illumination with a beam exit diameter of about 5 mm. The laser beam is shaped into a light sheet using a three lenses system, i.e., a diverging and a converging spherical lens (with focal length equal to -75mm and 100 mm, respectively), and a diverging cylindrical lens (with focal length equal to -100 mm). The resulting laser sheet thickness is less than 1 mm. The time separation between the two laser pulses is set to 200  $\mu\text{s}$  for the plane #2 while 40  $\mu\text{s}$  for the planes #1 and #3. Particle images are recorded by two Andor Zyla sCMOS cameras (2160px  $\times$  2560px, 16 bit, 6  $\mu\text{m}/\text{px}$ ) equipped with Scheimpflug adapters and Tokina objectives of 100mm focal length. The optical objective is set at numerical aperture  $f_{\#} = 16$  for the camera looking in forward scattering configuration (right camera in Figure 2) and  $f_{\#} = 8$  for the camera looking in backward scattering configuration (left camera in Figure 2), in order to compensate for the different brightness condition. The test campaign was conducted for the measurements of the three components of the velocity field on three different sectional planes #1, #2 and #3 shown in Figure 1(a) covering two consecutive slots. A region of approximately  $40 \times 30.5 D^2$  is imaged by the cameras yielding a final spatial resolution of 30.5 pixel/mm.

In order to perform phase-locked measurements, the acquisition system is synchronized with the SJ. The synchronization is performed by using a Digilent Inc. Analog Discovery. The input signal to the loudspeaker is used also as a trigger for the acquisition system. The acquisition system is set in order to sample the investigated phenomenon with a phase separation  $\Delta\varphi = 5^\circ$ . The sampling frequency is set to 10.410 Hz in order to obtain 72 phases describing the periodic phenomenon (see Greco et al. 2013). All the images are then processed with an in-house developed software to obtain reliable turbulent statistics based on the acquired 19440 double frame particles images (270 snapshots per phase).

An optical calibration is performed by recording images of a target mechanically translated along the spanwise direction ( $Z/D$ ) of the measurement volume in the range  $\pm 2$  mm. The final calibration error attains to a maximum value of 0.87 pixel. The misalignment between the calibration plate at  $Z/D = 0$  and the laser sheet is estimated by computing the disparity map based on the cross-correlation between the simultaneous dewarped images of the two cameras. The disparity attains to a maximum value of 0.55 mm. The quality of the images is improved by removing the unwanted background. The background images are estimated by computing the minimum of the intensity time series for each pixel of both frames.

The velocity field is computed with a multi-pass algorithm, windows deformation and Blackman weighting windows. The final interrogation window size is  $32 \times 32$  pixels with an overlap of 50%, thus

resulting in a vector pitch of 0.31 mm. A normalized median validation criterion is applied to remove spuriously detected vectors.

In this experiment, the particle image diameter attains to approximately 2.5 pixels, which is considered acceptable for a proper sampling of the particle image (Raffel et al. 2007). A rough estimate of the random error attains to a value of  $\sim 0.1$  pixel for real PIV images (Willert and Gharib 1991) and applying the method of propagation of errors (Bevington and Robinson 1969), the velocity field uncertainty is estimated approximately at 0.082 m/s, i.e., 3% of the longitudinal velocity component measured in the shear layer.

### 3 Results

In the following, the symbols  $U$ ,  $V$  and  $W$  indicate the velocity components along the  $X$ ,  $Y$  and  $Z$  directions, respectively. The corresponding lower-case letters  $u$ ,  $v$  and  $w$  refer to the components of the turbulent velocity fluctuations. The results are presented in dimensionless form, using the characteristic velocity  $U_0$  and the slot width  $D$  as reference quantities.

#### 3.1 Time average flow fields

The time-average flow field at the plane #1 is illustrated in Figure 3 by iso-contours of the velocity components  $\bar{V}/U_0$  (a),  $\bar{U}/U_0$  (b) and  $\bar{W}/U_0$  (c) with streamlines. The SJ exhibits an asymmetric spreading with respect to the geometrical axis of the slot; the streamlines in the shear layer at the far field are tilted of about  $\sim 14.8^\circ$  on the right side with respect to the vertical direction. This behavior can be ascribed by the design of the SJ actuator. In particular, the slots are located off-centered with respect to the maximum displacement of the piezo-electric diaphragm inducing an asymmetric development of the issuing jet about the slot axis. In Figure 3(a), a drop-like pattern of the SJ is clearly illustrated in proximity of the slot exit. It is elongated in longitudinal direction and featured by a maximum value of  $\sim 1.59$ . A small recirculation region with a minimum value of  $\sim -0.19$  is localized on the right side of the SJ core at the slot exit. The streamlines also indicate the entrainment process that advects fluid from the quiescent ambient to the SJ core. This effect is stronger at the slot exit as testified by the iso-contour of the crosswise velocity component  $\bar{U}/U_0$  shown in Figure 3(b). Further downstream, two lobed patterns of  $\bar{U}/U_0$  component are detected. Conversely, the fluid is ejected out from the SJ core with minimum and maximum values of  $\sim -0.47$  and  $\sim 0.81$ , respectively. The action on the right side is more prominent. In Figure 3(c), the out-of-plane velocity component  $\bar{W}/U_0$  exhibits a similar lobed pattern as described for the crosswise  $\bar{U}/U_0$  component. The maximum value is attained to 0.16, i.e., one order of magnitude lower than that measured for the crosswise  $\bar{U}/U_0$  component. On the other hand, the minimum value is reached at  $\sim -0.22$ , testifying an inversion of the SJ action along the out-of-plane direction.

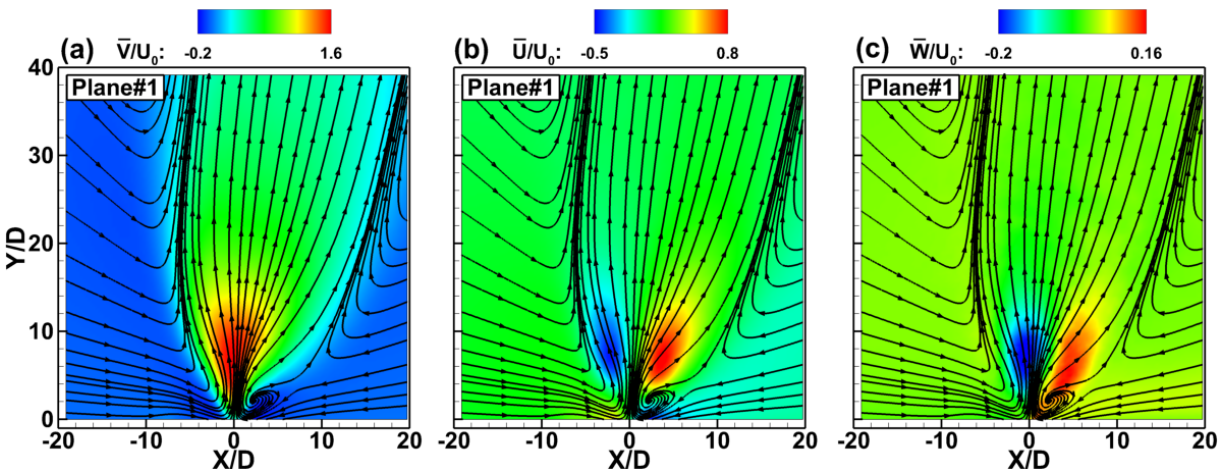


Figure 3 Iso-contours of time-average velocity components  $\bar{V}/U_0$  (a),  $\bar{U}/U_0$  (b) and  $\bar{W}/U_0$  (c) with streamlines at the plane #1.

In order to compare the flow pattern at different location of the SJ actuator, Figure 4 shows the iso-contours of the time-average velocity components with streamlines at the planes #2 (a, b and c) and #3 (d, e and f). At the plane #2 (in the mid distance between two consecutive slots), the longitudinal component exhibits a minimum value of  $\bar{v}/U_0 = -0.15$  in the proximity of the wall of the SJ actuator. Moving downstream, it continuously increases reaching a maximum  $\bar{v}/U_0 = 0.2$ . An entrainment of fluid coming from the quiescent ambient is observed from the inspection of both the streamlines and the crosswise time-average velocity component. In Figure 4(c), the out-of-plane velocity component is undetectable in the time-average map. This behaviour is also shown at plane #3 in Figure 4(f) in contrast with that has been observed at plane #1 in Figure 3(c). On the other hand, the longitudinal and crosswise time-average velocity components, illustrated in Figure 4(d) and (e), are characterized by similar patterns already described for the plane #1 (Figure 3(a) and (b)).

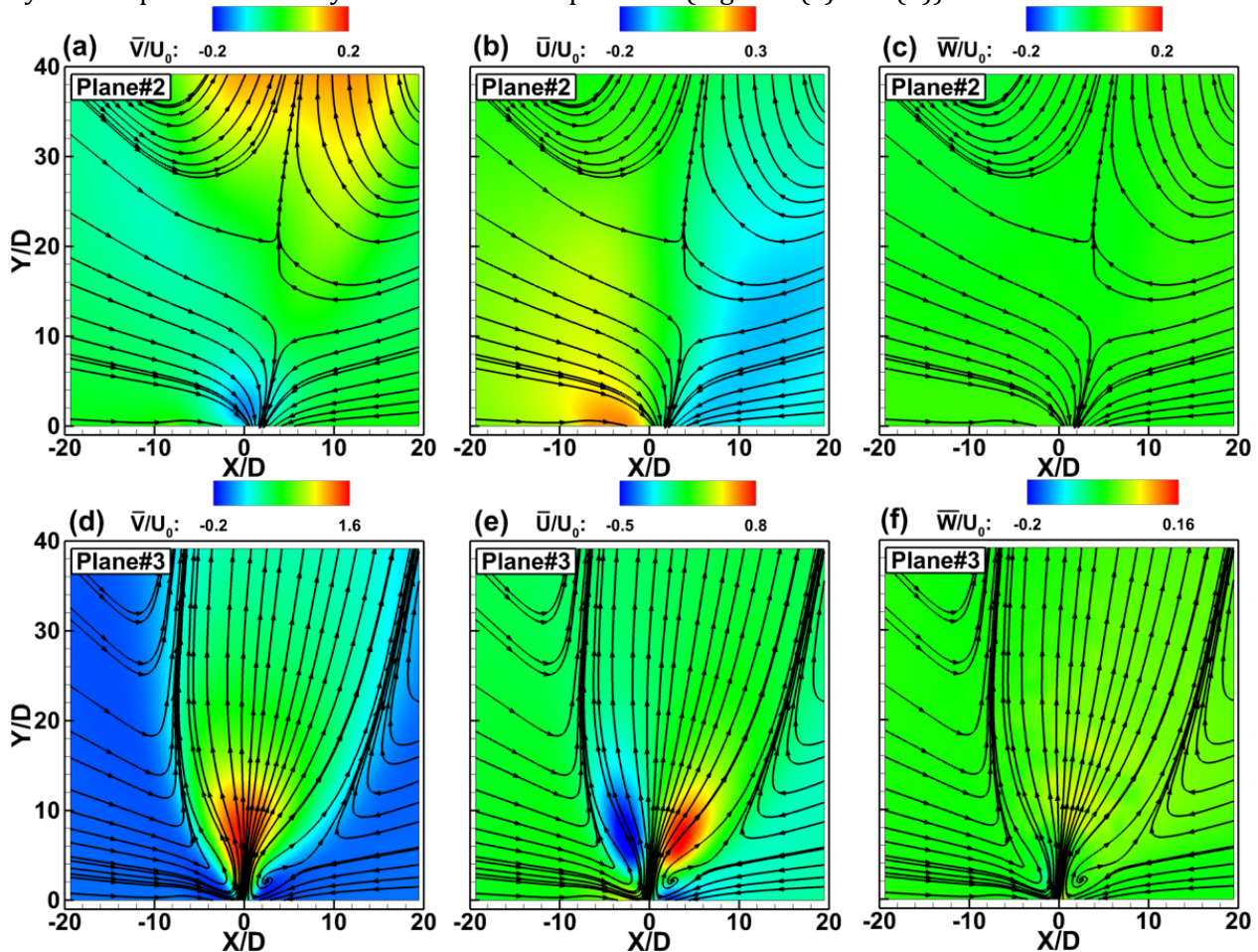


Figure 4 Iso-contours of time-average velocity components  $\bar{v}/U_0$  (a),  $\bar{u}/U_0$  (b) and  $\bar{w}/U_0$  (c) with streamlines at the planes #2 (a-c) and #3 (d-f).

The maps of the normal components of the Reynolds stress tensor  $\overline{v^2}/U_0^2$ ,  $\overline{u^2}/U_0^2$  and  $\overline{w^2}/U_0^2$  are depicted in Figure 5(a-c) and (d-f) for the planes #1 and #3, respectively. However, the level of turbulence at the plane #2 is negligible hence, for the sake of brevity, it has not been shown herein. The overall level of turbulence is located in the vicinity of the slot exit, the longitudinal component  $\overline{v^2}/U_0^2$  reaches a maximum value of  $\sim 1.1$  and extends along the longitudinal direction up to  $15D$  from the slot exit. The crosswise component  $\overline{u^2}/U_0^2$  exhibits an asymmetric spreading along the transversal direction featured by a lobed pattern with respect to the axis of the slot. For both planes #1 and #3, the maximum value of  $\overline{u^2}/U_0^2$  is attained to  $\sim 0.56$ . The out-of-plane component  $\overline{w^2}/U_0^2$  is

characterized by a drop-like shape, elongated in the longitudinal direction. At the planes #1 and #2, the intensity of the turbulence reaches maxima values of  $\overline{w^2}/U_0^2 = 0.39$  and  $0.35$ , respectively.

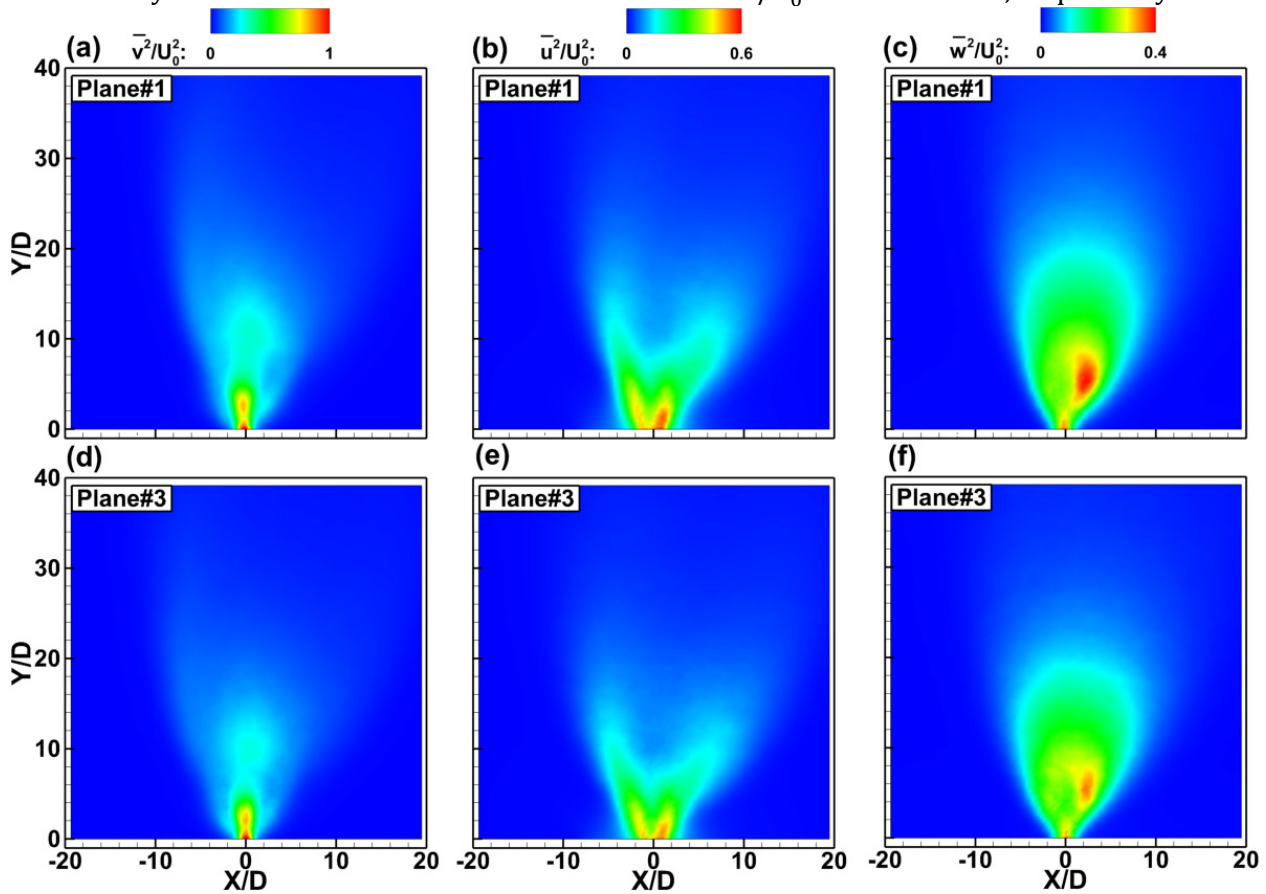


Figure 5 Iso-contours of the normal components of the Reynolds stress tensor  $\overline{v^2}/U_0^2$ ,  $\overline{u^2}/U_0^2$  and  $\overline{w^2}/U_0^2$  at the planes #1 (a-c) and #3 (d-f).

The iso-contours of the off-diagonal components of the Reynolds stress tensor  $\overline{uv}/U_0^2$ ,  $\overline{uw}/U_0^2$  and  $\overline{vw}/U_0^2$  are reported in Figure 6(a-c) and (d-f) for the planes #1 and #3, respectively. In Figure 6(a) and (d), a composite pattern of four peaks for the  $\overline{uv}/U_0^2$  shear stress is recognized in the near field of the SJ, i.e., up to approximately  $8D$  from the slot exit. The maps describe the entrainment occurring in the shear regions, two peaks of  $\overline{uv}/U_0^2 = -0.22$  and  $0.20$  are reached at the slot exit for both planes. Further downstream, the imprint of the  $\overline{uv}/U_0^2$  stress exhibits two local peaks symmetric with respect to the slot axis for values of  $-0.13$  and  $0.10$ . In Figure 6(b) and (e), the  $\overline{uw}/U_0^2$  shear stress features a peak at the slot exit of  $\overline{uw}/U_0^2 = 0.15$  for both planes and, further downstream, it spreads with more prominence along the longitudinal direction up to  $Y/D = 6.5$ . On the other hand, the  $\overline{vw}/U_0^2$  stress is characterized by maps with lower intensity, as illustrated in Figure 6(c) and (f). In addition, for the plane #1 the  $\overline{vw}/U_0^2$  stress exhibits two peaks of  $-0.050$  and  $0.052$  within the first  $20D$  from the slot exit along the slot axis. However, the longitudinal and out-of-plane components correlate with a negligible level of intensity for the plane #3.

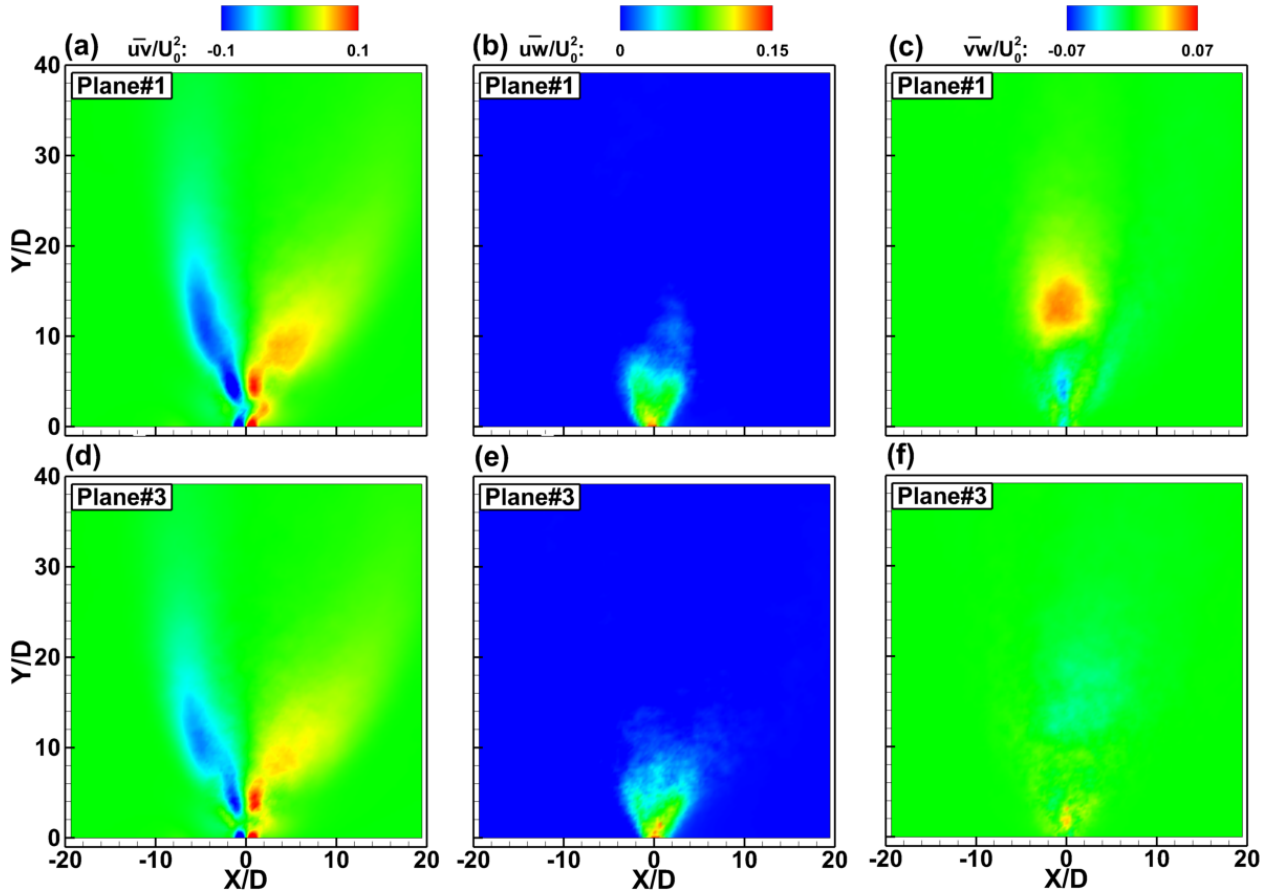


Figure 6 Iso-contours of the off-diagonal components of the Reynolds stress tensor  $\overline{uv}/U_0^2$ ,  $\overline{uw}/U_0^2$  and  $\overline{vw}/U_0^2$  at the planes #1 (a-c) and #3 (d-f).

### 3.2 Phase-average flow fields

In this section, the development of the SJ evolving in quiescent ambient is presented by phase-average flow fields. In the following, the phase-average operator is indicated by angle brackets  $\langle \cdot \rangle$ .

The iso-contours with in-plane velocity vectors of the longitudinal component  $\langle V \rangle / U_0$  of the phase-average velocity field are depicted in Figure 7. The maps feature in-plane velocity vectors with iso-lines of  $QD^2/U_0^2 = 0.2$  describing the vortex pattern. The Q-criterion (Q is the second invariant of the velocity gradient tensor) is used to visualize vortical flow features (Jeong and Hussain 1995). Figure 7(a) shows the beginning of the jet ejection that, in this argumentation, has been chosen as the reference starting event indicated by  $\varphi = 0^\circ$ . A vortex is located at  $Y/D = 7.1$  between the SJ and the quiescent ambient; a burst of fluid advects along the longitudinal direction with longitudinal velocity  $\langle V \rangle / U_0 = 2.1$ . At  $\varphi = 50^\circ$  (Figure 7(b)), an ejection of fluid is detected at the slot exit with  $\langle V \rangle / U_0 = 1.2$  whereas the peak of  $\langle V \rangle / U_0$  moves further downstream at  $Y/D = 9.8$ . At  $\varphi = 100^\circ$ , the fluid ejected from the slot determines two peaks of negative longitudinal velocity  $\langle V \rangle / U_0 = -0.97$  induced by the roll-up of the shear layer. Increasing the phase up to  $\varphi = 150^\circ$ , the map is featured by a peak of longitudinal velocity of  $\langle V \rangle / U_0 = 1.7$  at  $Y/D = 3.4$ . At  $\varphi = 200^\circ$ , the vortex pattern is fully developed. The induction of the vortex determines a peak of  $\langle V \rangle / U_0 = 3.0$  at  $Y/D = 3.4$  and a different spreading of the SJ itself along the longitudinal direction. The suction cycle starts approximately at  $\varphi = 225^\circ$  characterized by negative longitudinal velocity at the slot exit, simultaneously, further downstream, a saddle point (i.e. where the in-plane velocity vector is approximately zero) is recognized at  $Y/D = 1.1$ . At  $\varphi = 270^\circ$  (Figure 7(f)), the vortex pattern loses its coherence on the right side of the slot axis and the peak of the longitudinal velocity component decreases down to  $\langle V \rangle / U_0 = 2.2$ .

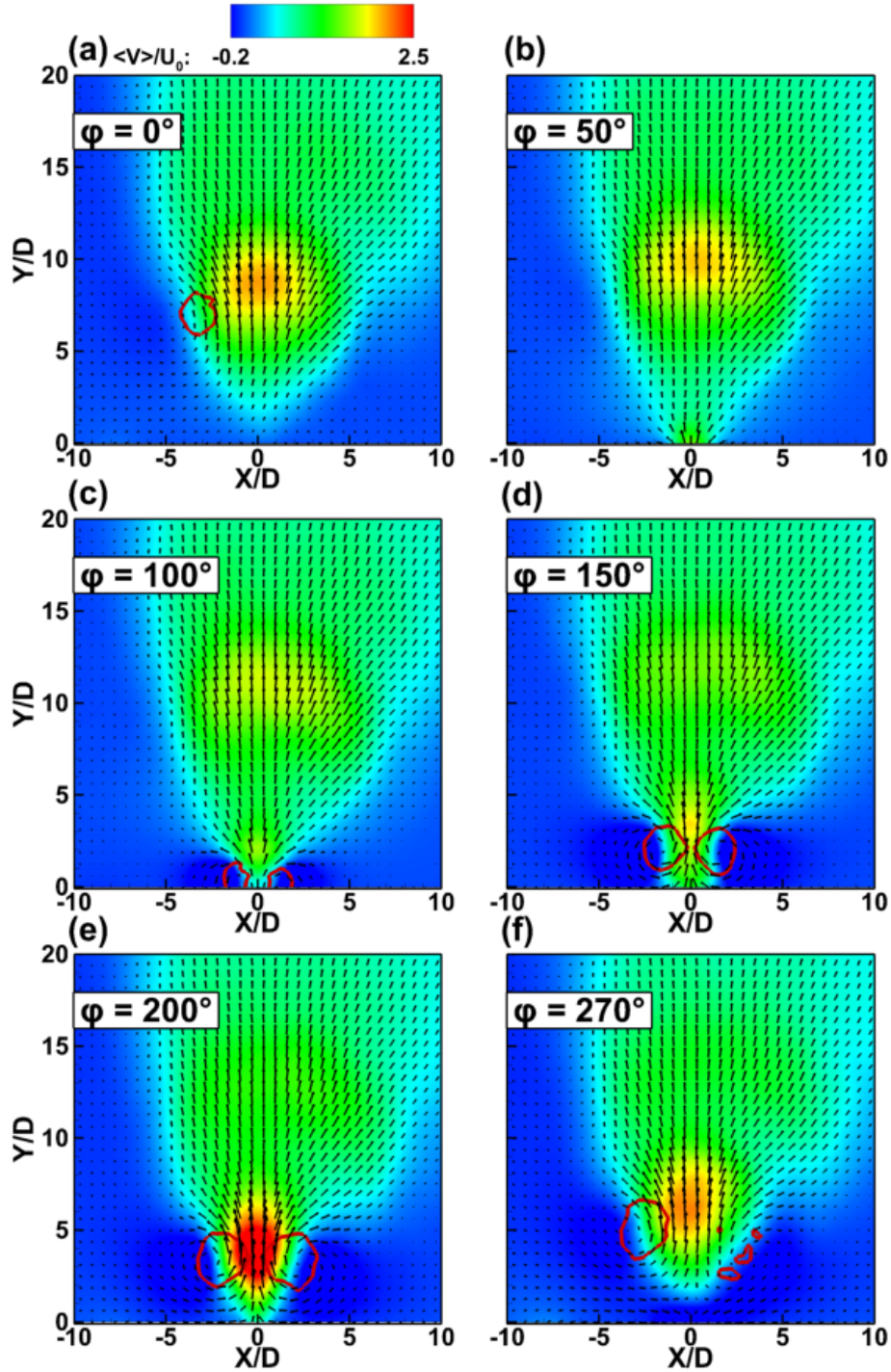


Figure 7 SJ evolution: iso-contours of the longitudinal phase-average velocity component  $\langle V \rangle / U_0$  with in-plane velocity vectors describing the SJ development at different phases for the plane #1. Vortex visualization using Q-criterion: iso-lines of  $QD^2 / U_0^2 = 0.2$ .

The main flow features at the plane #2 are illustrated in Figure 8 with maps of  $\langle V \rangle / U_0$ ,  $\langle U \rangle / U_0$  and turbulent kinetic energy  $\langle TKE \rangle / U_0^2$  at the phases  $\varphi = 10^\circ$  (a-c) and  $150^\circ$  (d-f), respectively. Where  $\langle TKE \rangle$  is defined herein as formulated in Eq. 2.

$$\langle TKE \rangle = \langle u^2 \rangle + \langle v^2 \rangle + \langle w^2 \rangle \quad (2)$$

The flow is characterized by the presence of a saddle point which is denoted by a white spot in Figure 8. At  $\varphi = 10^\circ$  (Figure 8(a-c)), the maps of  $\langle V \rangle / U_0$  and  $\langle U \rangle / U_0$  indicate entrainment of fluid coming from the quiescent ambient ( $Y/D = 21$ ) down to the SJ wall. Further downstream, the flow exhibits a more complex pattern testified by the level of  $\langle TKE \rangle / U_0^2 = 0.019$ . Increasing the phase up to  $\varphi = 150^\circ$ , the saddle point moves more upstream at  $Y/D = 6.1$ . The entrainment process is reduced in size and the fluid advects further downstream. A complex flow pattern is still detected at  $Y/D > 20$  with an intensified level of turbulence.

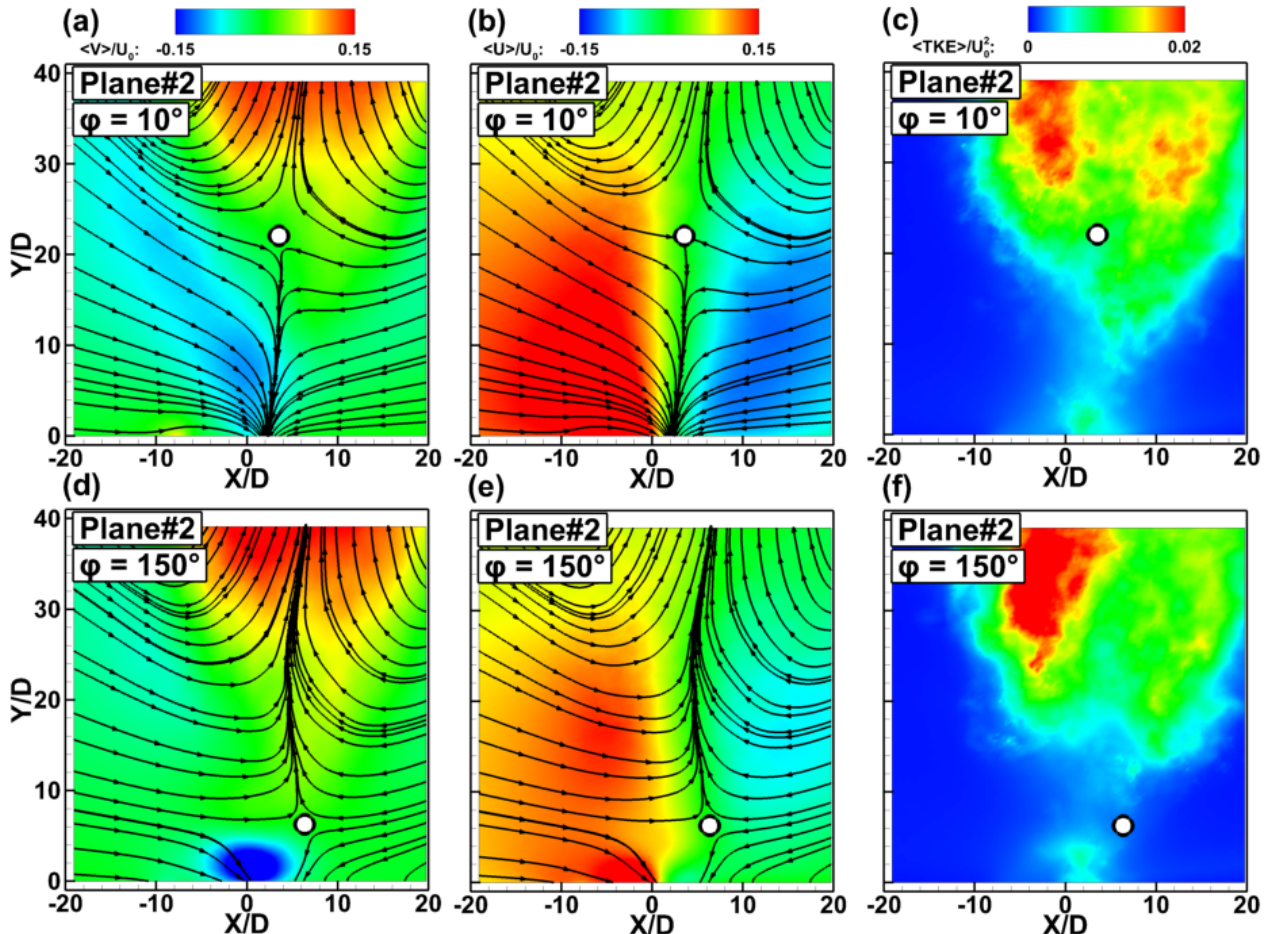


Figure 8 Iso-contours of phase-average velocity components  $\langle V \rangle / U_0$ ,  $\langle U \rangle / U_0$  and turbulent kinetic energy  $\langle TKE \rangle / U_0^2$  with streamlines at the phases  $\varphi = 10^\circ$  (a-c) and  $150^\circ$  (d-f), respectively, on the plane #2. The white spot indicates the saddle point.

## 4 Conclusions

An experimental investigation of the flow field at the exit of a multi-slotted array of SJ issuing in quiescent ambient at Reynolds number  $Re = 128$  and Strouhal number  $St = 0.11$  has been carried out by means of phase-locked S-PIV measurements. Multi-slotted SJ actuator was composed of twelve rectangular slots with an aspect ratio of 15 (for a width of  $\sim 1$  mm) and off-centered with respect to the cavity center. Experiments were conducted at three equally spaced planes aligned along the slot width. Two planes are located at either two consecutive slot exit; an additional measurement was performed at the mid-distance between them.

At the slot exit, the time-average flow fields reveal that the SJ exhibits an asymmetric spreading with respect to the geometrical axis of the slot. A small recirculation region is detected slightly downstream of the slot exit where the cavity extends; the flow is tilted in average of about  $14.8^\circ$  towards the cavity. On the other hand, the flow field appears to be two-dimensional at the mid spanwise distance between two consecutive slots. The phase-locked flow fields exhibit counter-rotating vortical

structures that move downstream from the slot exit during the ejection phase. These vortices develop up to  $3.4 D$  in the longitudinal direction and then dissipate by the time they travel further downstream.

## Acknowledgements

This research has been supported by the Italian Aerospace Research Center (CIRA) and conducted in collaboration with the Department of Industrial Engineering (DII, University of Naples 'Federico II') as part of the synthetic jet actuators for flow control (SHAFT) project.

## References

- Amitay M, Smith BL, and Glezer A (1998) Aerodynamic flow control using synthetic jet technology. AIAA Paper 1998-0208  
doi: 10.2514/6.1998-208
- Bevington, PR, and Robinson, DK (2003) *Data Reduction and Error Analysis for the Physical Sciences*. Chapter 2 Probability Distribution, page 36. McGraw-Hill. 3rd edition
- Chiatto M, Capuano F, Coppola G, and De Luca L (2017) LEM Characterization of Synthetic Jet Actuators Driven by Piezoelectric Element : A Review. *Sensors* 17:1216  
doi: 10.3390/s17061216
- Chiatto M, Palumbo A, and De Luca L (2019) Design approach to predict synthetic jet formation and resonance amplifications. *Experimental thermal and fluid science* 107:79-87  
doi: 10.1016/j.expthermflusci.2019.05.013
- Glezer A (2011) Some aspects of aerodynamic flow control using synthetic-jet actuation. *Philosophical Transactions of the Royal Society A* 369:1476–1494  
doi: 10.1098/rsta.2010.0374
- Glezer A, and Amitay M (2002) Synthetic Jets. *Annual Review of Fluid Mechanics* 34:503–509  
doi: <https://doi.org/10.1146/annurev.fluid.34.090501.094913>
- Greco CS, Ianiro A, Astarita A, and Cardone G (2013) On the near field of single and twin circular synthetic air jets. *International Journal of Heat and Fluid Flow* 44: 41–52.  
doi: <https://doi.org/10.1016/j.ijheatfluidflow.2013.03.018>
- Ho C, and Tai Y (1996) Review: MEMS and Its Applications for Flow Control. *Journal of Fluids Engineering* 118:437–447  
doi: 10.1115/1.2817778
- Jeong J, and Hussain F (1995) On the identification of a vortex. *Journal of Fluid Mechanics* 285:69–94
- Palumbo A, Chiatto M, and De Luca L (2018) Measurements versus Numerical Simulations for Slotted Synthetic Jet Actuator. *Actuators* 7:59  
doi: 10.3390/act7030059
- Raffel M, Willert CE, Wereley ST, and Kompenhans J (2007) *Particle Image Velocimetry - A Practical Guide*. Chapter Image evaluation methods for PIV, page 164. Springer. 2nd edition
- Sahni O, Wood J, Kenneth E, and Amitay M (2011) Three-dimensional interactions between a finite-span synthetic jet and a crossflow. *Journal of Fluid Mechanics* 671:254–287  
doi: 10.1017/S0022112010005604
- Smith BL, and Glezer A (1998) The formation and evolution of synthetic jets. *Physics of Fluids* 10:2281–2297  
doi: 10.1063/1.869828
- Willert C (1999) Stereoscopic digital particle image velocimetry for application in wind tunnel flows. *Measurements Science and Technology* 8:1465–1479  
doi: 10.1088/0957-0233/8/12/010
- Willert CE, and Gharib M (1991) Experiments in Fluids Digital particle image velocimetry. *Experiments in Fluids* 10:181–193  
doi: 10.1007/s00348-012-1280-x